The Polarity of Co-solvents Regulates the Charge Storage Mechanisms in Supercapacitors with Concentrated Electrolytes

Murillo L. Martins[1], Tao Wang[2,3], Sheng Dai[2,3], Eugene Mamontov[1]

[1] Neutron Scattering Division, Oak Ridge National Laboratory, PO BOX 2008 MS6455, Oak Ridge, Tennessee 37831, United States
[2] Chemical Sciences Division, Oak Ridge National Laboratory, Oak Ridge, TN, 37831, USA
[3] Department of Chemistry, Institute for Advanced Materials and Manufacturing, University of Tennessee, Knoxville, TN, 37996, USA

TOC Graphic

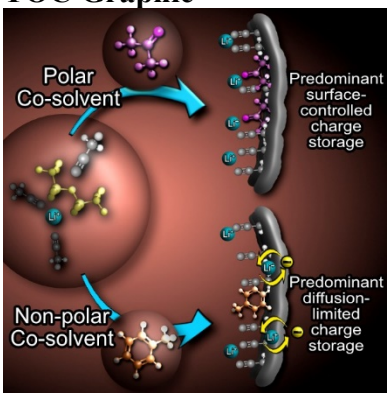

Abstract

Developing better energy storage devices depends on comprehending the underlying mechanisms involved in charge storage. With the continuous conception of new electrolytes, this task becomes progressively more urgent and complex. An example is the utilization of co-solvated concentrated solutions. While these show promising electrochemical responses, their dynamic properties (especially under confinement) and their relationships with the performance, are not fully understood. Here, we combined a modified step potential electrochemical spectroscopy (SPECS) and quasielastic neutron scattering (QENS) to investigate systems composed of activated mesoporous carbon (AMC) and concentrated solutions of Lithium bis(trifluoromethanesulfonyl)imide in acetonitrile co-solvated with either toluene or acetone. We report that acetone does not impair surface-controlled mechanisms, contrarily to toluene which competes with charged species to populate the AMC's pores without contributing to charge storage. In turn, toluene promotes a greater overall capacitance owing to Faradaic processes, which may be related to changes in the solvation structures under confinement.

Main

The development of safer and more efficient energy storage devices intimately depends on the comprehension of the underlying mechanisms involved in charge storage in confined geometries.[1] Traditionally, charge storage is regarded as either based on charge induction (non-Faradaic) or transfer (Faradaic mechanisms).[2] More recently, a continuum between these mechanisms has been proposed, which accounts for the roles played by the geometry and chemical environment of the electrochemical interfaces, the nature of the electrolytes, and, most importantly, the interplay between these factors.[3] From the standpoint of the latter, strong ion solvation generally favors electrostatic interactions with the electrode surfaces, and thus the induction of charge. Meanwhile, partial and/or complete desolvation, which may be promoted by confinement, allows for chemical bonding between the ions and the electrodes.[4, 5]

An extra complexity to this picture is brought by the rising utilization of concentrated electrolytes. Despite their promising properties,[6-11] the dynamics and structure of ions, solvents, and the correspondent solvation complexes are yet to be fully understood especially under confinement in electrode materials.[12-15] Additionally, there is a growing use of co-solvation strategies to mitigate drawbacks related to the viscosity and salt precipitation in these concentrated electrolytes, which leads to even more complex solvation structures.[16-25]

The initial concept of co-solvation is based on adding nearly inert molecules able to reduce the solution's viscosity while preserving the ion-ion and ion-solvent correlations found in the original concentrated system.[26-30] By doing so, the often-called locally concentrated electrolytes are conceived. Nevertheless, as recently observed in bulk solutions of Lithium bis(trifluoromethanesulfonyl)imide (LiTFSI) in acetonitrile (C_2H_3N), even co-solvents with low dielectric constants (e.g. chloroform, toluene, and dichloromethane) that do not directly engage in

the ionic solvation, experience drastic decreases in diffusivity associated with long-range interactions with the ions. Also, despite lowering the viscosities, adding these co-solvents leads to a decrease in the room-temperature conductivities owing to changes in the overall ion-ion correlations. With a co-solvent with a moderate dielectric constant, e.g. acetone, the room temperature conductivity of the solution does increase and most of the ion-ion interactions remain unchanged. However, since the co-solvent engages in ionic solvation, larger ion-solvent complexes are formed, which may have consequences in the intercalation and adsorption of ions.[27-29]

While the above-described results highlight that the effects of co-solvation can be far more complex than expected, this knowledge is still mostly restricted to bulk systems. Therefore, the behavior of these co-solvents under confinement and ultimately its relationship with the electrolyte's electrochemical performance needs further investigation. In this work, we evaluated the electrochemical performances of concentrated solutions of LiTFSI in acetonitrile (LiTFSI/acetonitrile = 3:1 molar ratio) co-solvated with either acetone (C_3H_6O) or toluene (C_7H_8) in activated mesoporous carbon (AMC) electrodes. Our main focus is to decipher the underlying mechanisms that drive the electrochemical responses and, for this, we combined a modified step potential electrochemical spectroscopy (SPECS)[31, 32] and quasielastic neutron scattering (QENS).[33, 34] With the first, we assessed the contributions of different energy storage mechanisms to the overall capacitance of the system. With QENS, the unique penetrating power of neutrons allowed us to evaluate the dynamics of acetonitrile and the co-solvents under confinement. To individually assess the dynamics of these species and relate them with the electrochemical responses, we harnessed the exceptionally higher incoherent neutron scattering cross-section[34] of

^{1}H in comparison with ^{2}D and performed selective deuteration of either acetonitrile or the co-solvents.

In this work, we used sodium amide-activated mesoporous carbon as our electrodes/confinement matrix. The synthesis and pore properties were previously reported in ref. [31]. In brief, the total surface area of this AMC is 1133 m^2/g as determined via N_2 adsorption experiments. The detailed pore structure of the matrix was calculated with non-localized density functional theory (NLDFT) analysis and it has been determined that the hierarchical structure is divided as follows: ~ 32% of the pore area corresponds to micropores with sizes < 1 nm, ~ 44 % corresponds to micropores with sizes ranging between 1 and 2 nm, and mesopores with sizes between 2 and 10 nm account for ~ 24% of the pore area. The NLDFT results are reproduced from ref. [31] in Fig. S1. As for the co-solvated solutions, they were both prepared to present a final concentration of 5.5 mol/kg (mols of salt per weight of the solvents) and are hereafter named Solution A when co-solvated with acetone, and Solution T, when co-solvated with toluene. To achieve the final concentration in mol/kg the molar ratios for each solution are as follows: Solution A: LiTFSI/acetonitrile/acetone = 1:3:1 and Solution T: LiTFSI/acetonitrile/toluene = 1:3:0.63. Additional details on samples preparation are given in the Supplementary Information (SI). Note that, as reported in ref. [27], the viscosities of the obtained solutions are very much comparable. The SPECS results show that Solution T allows for improved specific capacitance, mostly because of a much-enhanced contribution from diffusive processes. Meanwhile, Solution A allows for larger surface-controlled storage mechanisms. These results were rationalized by the QENS experiments, which revealed that, despite the low dielectric constant, toluene does compete with charged species to populate the AMC's hierarchical structure, which hinders surface-controlled charge storage. Overall, the diffusivities of the solvents under confinement are higher than those previously

reported for the bulk solutions,[27] which suggests a partial breakdown of the original solvation complexes. This is particularly critical for toluene, whose high diffusivity points to sluggish interaction with ions, which may be decisive for the occurrence of diffusion-controlled mechanisms.

In Fig.1a and b, cyclic voltammetry (CV) curves under scan rates between 1 and 100 mV/s for the AMC (for synthesis details, see SI) with Solutions A or T are presented, and Fig.1c highlights the CV curves obtained with each solution at 10 mV/s, which reveal larger redox peaks and decomposition currents in Solution T. According to our previous work using the SPECS method, the redox peaks correspond to the capacitance contributions from diffusion processes, [31] which are also referred to as pseudocapacitance. Regarding the decomposition current, it either arises from the electrolyte decomposition or the corrosion of current collectors. The specific capacitances calculated from the CV curves are displayed in Fig.1d as functions of the scan rate, and one can notice the higher specific capacitance provided by Solution T, while a better rate performance is achieved with Solution A.

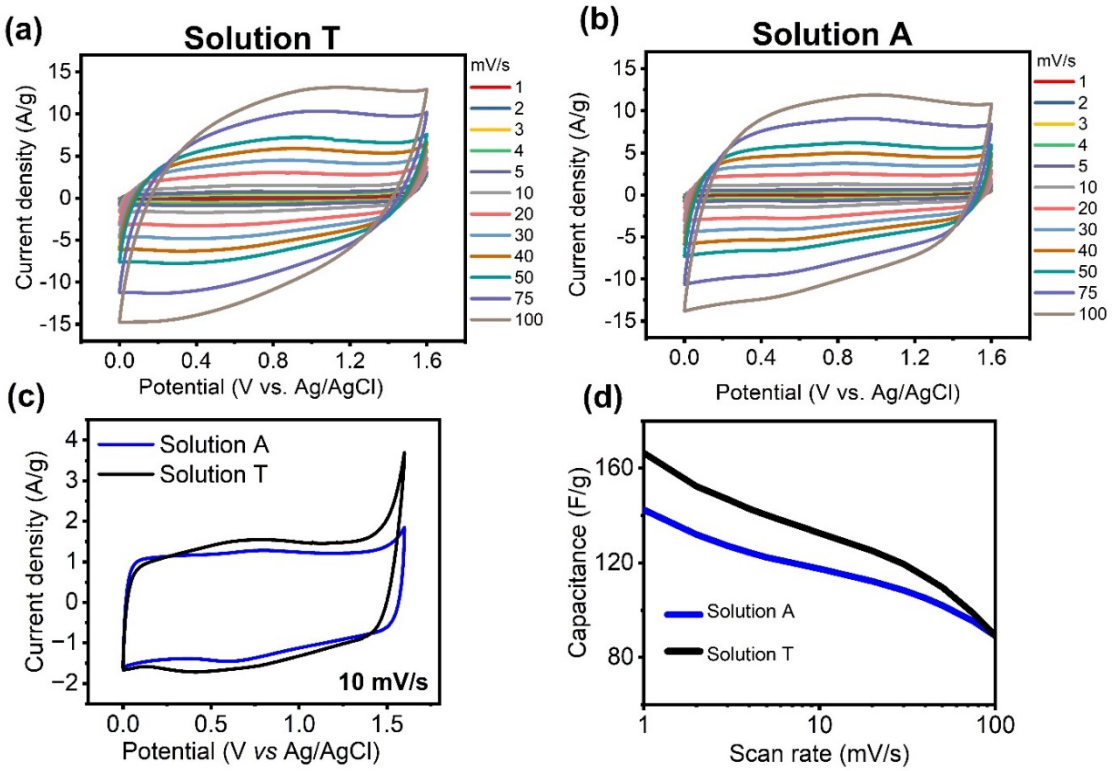

Fig. 1. In (a) and (b) CV curves at different scan rates from 1 to 100 mV/s for the systems with Solutions A and T are shown. In (c), the CV curves at 10 mV/s are depicted and (d) shows the specific capacitances at different scan rates calculated from the CV curves.

With SPECS, we broke down the different contributions for the transit current within the electrode. These experiments were performed by applying a staircase potential with 50 mV steps and an equilibration time of 300 s (Fig. S2). At each step, the specific current was recorded as a function of time (Fig. S3) and the current response from capacitive processes (i_C) is described as:

$$i_C = \frac{\Delta E}{R} exp\left(-\frac{t}{RC}\right) \qquad (1)$$

where ΔE is the potential step, R is the series resistance (Ω.g), C is the double-layer capacitance (F/g), and t is the time after the potential step. The current responses from double-layer formation on different pore geometries (i_{Macro}, i_{Meso}, and i_{Micro}) were differentiated based on the distinct time constants (τ = RC; s). That is, micropores have the highest series resistance because of the

restricted ion transport and/or partial ionic desolvation. Meanwhile, the resistance in mesopores is only slightly larger than in the macropores, because both are large enough to be accessed by solvated ions. However, the much larger surface area of mesopores (Fig. S1) allows for a greater capacitance and ultimately a much larger time constant ($\tau_{Meso} > \tau_{Macro}$).

The current response from diffusion-limited processes (i_D) is also included in the SPECS analyses and is modeled using the Cottrell equation:

$$i_D = nFAc\left(\frac{D}{\pi t}\right)^{1/2} \quad (2)$$

Where n is the number of electrons transferred, F is the Faraday constant (96485 C/mol), A is the electrochemically active surface area (m^2/g), c is the concentration of electro-active species (mol/m^3), and D is the diffusion coefficient (m^2/s). In the end, the overall current response is described as the sum of the three contributions from double-layer charging processes (i_{Macro}, i_{Meso}, and i_{Micro}), i_D, and a residual equilibrium current (i_R) accounting for electrolyte decomposition and/or corrosion of current collectors. Then, eqs. 1 and 2 can be combined as:

$$i(t) = i_{\mathrm{Macro}} + i_{\mathrm{Meso}} + i_{\mathrm{Micro}} + i_{\mathrm{D}} + i_{\mathrm{R}}$$

$$= \frac{\Delta E}{R_{\mathrm{Macro}}}\exp\left(-\frac{t}{R_{\mathrm{Macro}}C_1}\right) + \frac{\Delta E}{R_{\mathrm{Meso}}}\exp\left(-\frac{t}{R_{\mathrm{Meso}}C_2}\right) + \frac{\Delta E}{R_{\mathrm{Micro}}}\exp\left(-\frac{t}{R_{\mathrm{Micro}}C_3}\right) + \frac{B}{t^{1/2}} + i_R \quad (3)$$

In eq.3, the term B consolidates all the constants in eq.2 and, together with C_1, C_2, C_3, R_{Macro}, R_{Meso}, R_{Micro}, and i_R, is obtained by nonlinear fitting of the data.[31, 32] As shown in Fig. 2a, Solution A promotes greater surface-controlled charge storage regardless of the pores' dimensions, although this feature is particularly remarkable in the mesopores. In turn, as shown in Fig.2b, Solution T allows for a remarkably higher charge storage contribution from diffusion-limited processes, which ultimately leads to a higher capacitance obtained with this electrolyte. As shown in Figure

S5, the capacitance contribution from residual current in Solution T is also higher than that in Solution A.

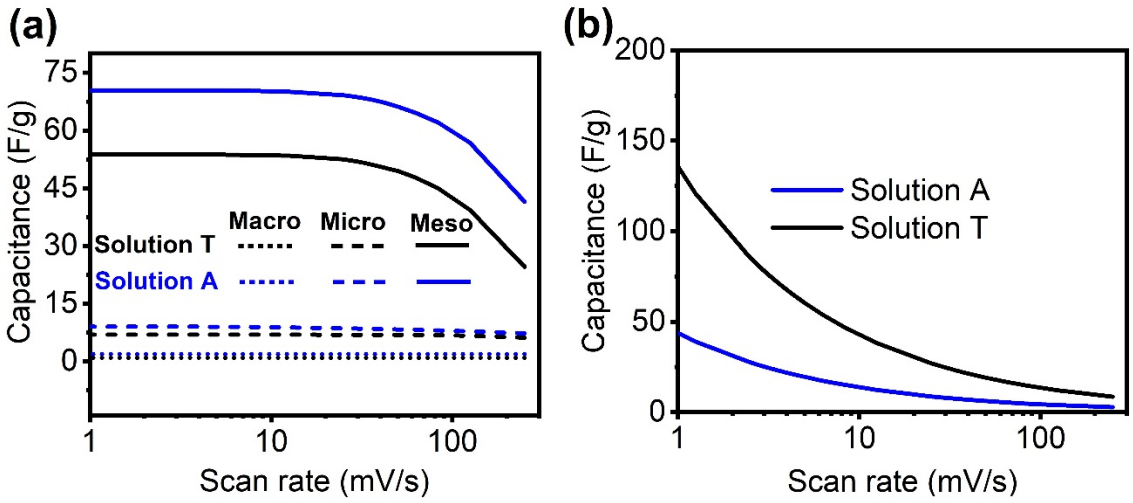

Fig. 2. SPECS analysis for hyper porous carbon in acetonitrile/LiTFSI concentrated solutions co-solvated with toluene and acetone. (a) Breakdown capacitances from macro, meso, and micropores for each electrolyte. (b) Capacitances contributions from diffusion processes.

Next, we used QENS to unravel the roles played by acetonitrile and the co-solvents in the charge storage mechanisms revealed by SPECS. With QENS we investigate the momentum and energy exchange (Q, ω) between neutrons and atoms within the ns to ps timescale (considering the BASIS spectrometer used in this work – for more details see SI). Namely, QENS probes the incoherent scattering of neutrons after interacting with a sample and, therefore, depicts the single-particle dynamics within the system. Since acetonitrile and the co-solvents used in this work are hydrogenated species, we explore the exceptionally higher incoherent neutron scattering cross-section of ^{1}H in comparison with any other isotope, including ^{2}D, to measure the dynamics of each compound.[34] For this, we measured electrolytes bearing either protiated acetonitrile with the deuterated co-solvent or deuterated acetonitrile with the protiated co-solvents. In the following lines, the protiated compounds, whose responses dominate the QENS signals, are designated by the index "*p-"* whereas the deuterated ones are labeled with *"d-"*. An additional feature of QENS

is the temperature-dependent energy-resolved "elastic" scattering intensity scans, shown in Fig.3a. The intensities of these scans are directly proportional to the concentration of ^{1}H atoms whose energy exchange with the neutrons beam is below the instrument's resolution. That is, it reflects the concentration of ^{1}H-atoms that is either immobile or only performs motions slower than a few nanoseconds.[35] For better statistics, the scans are presented as sums of the data collected between Q = 0.5 – 1.1 Å^{-1}. In the inset of Fig.3a, the data are normalized by the number of ^{1}H-atoms at each molecule and the data points at the lowest temperatures give a qualitative perspective of the amount of each solvent adsorbed into the AMC pores. From this analysis, the total number of molecules of acetonitrile plus co-solvents is nearly the same in both solutions but the ratios between the species are different. In Solution A, we estimate an acetonitrile/acetone ~ 2:1 molar ratio, and in Solution T we have acetonitrile/toluene ~ 3:1. Note that, in both cases, part of the acetonitrile content is likely loosely adsorbed in the AMC and is removed during sample preparation (see SI).

In Figs.3b and c, the scans presented in Fig.3a are reproduced but with the data at the lowest temperature points normalized to unity. With this representation, we evaluate the fraction of ^{1}H-atoms whose dynamics enter the spectrometer's timescale and cause deviations in the monotonical temperature-dependent decrease in intensity. In Fig. 3b, the data for Solution A are presented and the absence of abrupt drops in the elastic intensity scans indicates that no freezing-melting transitions are detected neither from *p*-acetonitrile nor *p*-acetone, demonstrating that we are majorly probing confined dynamics. Also, both *p*-acetonitrile and *p*-acetone present activation of dynamic motions at ~ 270 K. Once we compare the data points at room temperature, we observe that the fractions of elastic scatters are comparable for *p*-acetonitrile and *p*-acetone. As for Solution T, Fig.3c, *p*-acetonitrile presents detectable dynamics at ~ 260 K, whereas *p*-toluene presents an additional slight onset in the elastic intensity scans at ~ 185K. This temperature is close to toluene's

melting point (178K),[36] indicating that a fraction of this co-solvent may exist as a bulk-like population within the sample. Still, a clear melting-freezing transition is not observed. At room temperature, the fraction of elastic scatters is larger for *p*-acetonitrile than for *p*-toluene.

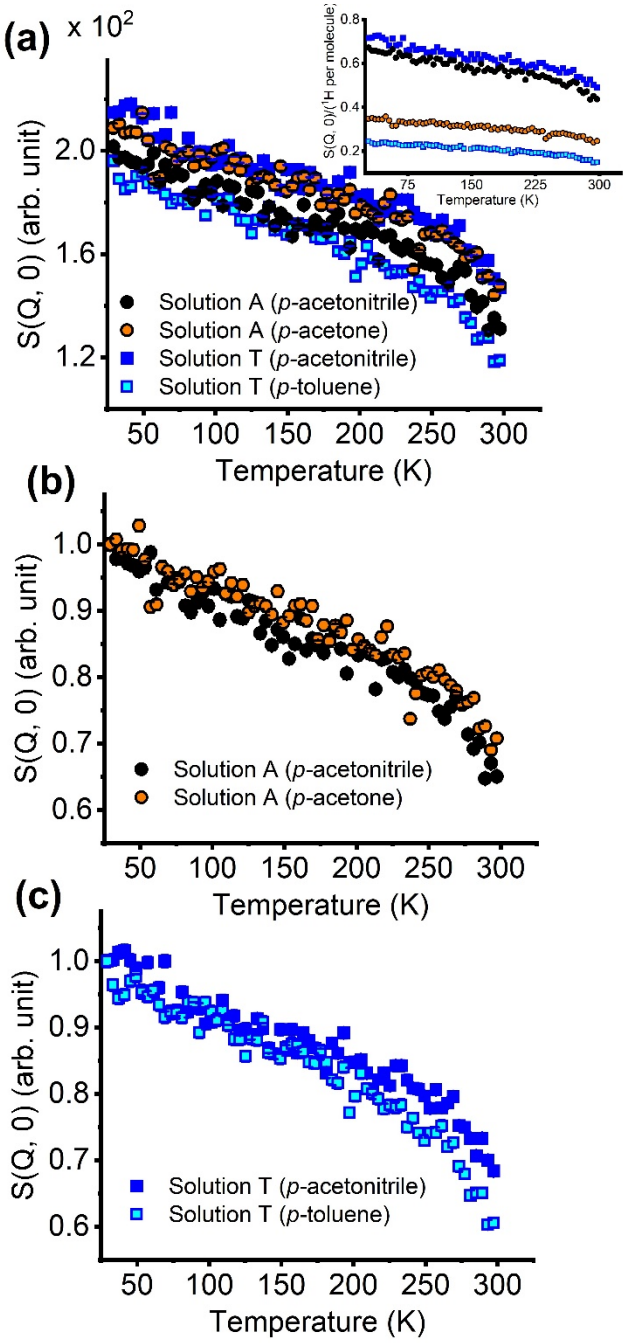

Fig. 3. In (a), temperature-dependent neutron elastic scattering intensity scans for Solutions A and T. The protiated compounds are indicated in the captions. The inset shows the data normalized by the number of ^{1}H-atoms per molecule. In (b), the data for Solution A are normalized by the data

point at the lowest temperature, and a similar representation is shown in (c) for Solution T. For better visualization, all the results are presented as the sums of the data collected between Q = 0.5 – 1.1 $Å^{-1}$.

Guided by the results presented in Fig.3, full QENS spectra were collected at 260 K, 280 K, and 300 K and their dependence on momentum and energy exchange can be described as:

$$I(Q,\omega) = [A_0(Q)\delta(\omega) + (1 - A_0(Q))S(Q,\omega)] \otimes R(Q,\omega) + B(Q,\omega) \quad (4)$$

where $A_0(Q)$ is the fraction of elastic scattering, $\delta(\omega)$ is a Dirac delta function that accounts for the elastic scattering (zero energy transfer), $S(Q,\omega)$ is the model dynamic scattering function, $R(Q,\omega)$ is the instrument resolution function (details in the SI), and $B(Q,\omega)$ is a linear background. In Fig.4a, the evolutions of $A_0(Q)$ at 300K go along with the data shown in Fig.3 (at the highest temperatures) but with better statistics (the results obtained at 260 and 280 K are presented in the SI). In Solution A, the immobilized (and/or drastically slowed-down) fractions of *p*-acetonitrile and *p*-acetone are very similar and account for ~ 85% of the ^{1}H-atoms of each compound. Meanwhile, in Solution T, the elastic fraction of *p*-acetonitrile is comparable to that in Solution A and, despite the low dielectric constant, toluene does interact strongly with the pore walls and has ~80% of its ^{1}H-atoms solely contributing to the elastic fraction of the QENS data. Here, we can reasonably consider that the dipolar character of acetonitrile and acetone still allows for the coordination of Li^+ even when these solvents are immobilized on the carbon interfaces.[37] In contrast, toluene's immobilization by the AMC walls merely creates competition with charged species for occupying the electrode pores without contributing to charge storage. Therefore, considering the acetonitrile/co-solvent molar ratios estimated from Fig.3a (acetonitrile/toluene = 3:1 for Solution T), ~ 25% of the molecules immobilized at room temperature in Solution T do not contribute to surface-controlled charge storage. In good agreement with these considerations, the

surface-controlled capacitance in Solution T is ~ 24% lower than the one found in Solution A (Fig.2a).

Turning to the dynamic scattering function in eq. 4, $S(Q,\omega)$, it describes the mobile fraction of the ^{1}H-atoms in each protiated solvent. Using the qClimax software,[38] the $S(Q,\omega)$ were fitted with a single Lorentzian function:

$$S(Q,\omega) = \frac{1}{\pi}\frac{\Gamma(Q)}{\Gamma^2(Q) + \omega^2} \quad (5)$$

where Γ(Q) is the half-width at the half-maximum of the QENS signal, and its Q-dependence was then fitted with a jump-diffusion model:[39]

$$\Gamma(\mathrm{Q}) = \frac{\hbar D Q^2}{1 + DQ^2\tau_0} \quad (6)$$

Where $\hbar$ is the reduced Planck's constant, τ_0 is the residence time between jumps, and D is the diffusion coefficient. In Fig.4b, the fits of Γ(Q) obtained at 300 K are shown and similar analyses for the data collected at 260 K and 280 K are presented in the SI. In Fig.4c, the diffusivities obtained for each solvent at 260 K, 280 K, and 300 K are displayed and do not follow a continuous increase with temperature because motions within more constrained geometries are gradually activated and contribute to the average detected diffusivities. Also, as elaborated further in the manuscript, the temperature-dependent evolution of the diffusion coefficients is strongly affected by the fraction of immobile molecules from each solvent at a given temperature. For example, in Solution T, *p*-acetonitrile is only faster than *p*-toluene at 260 K, when a very small fraction fraction of the molecules of the former is mobile (see Fig. S8).

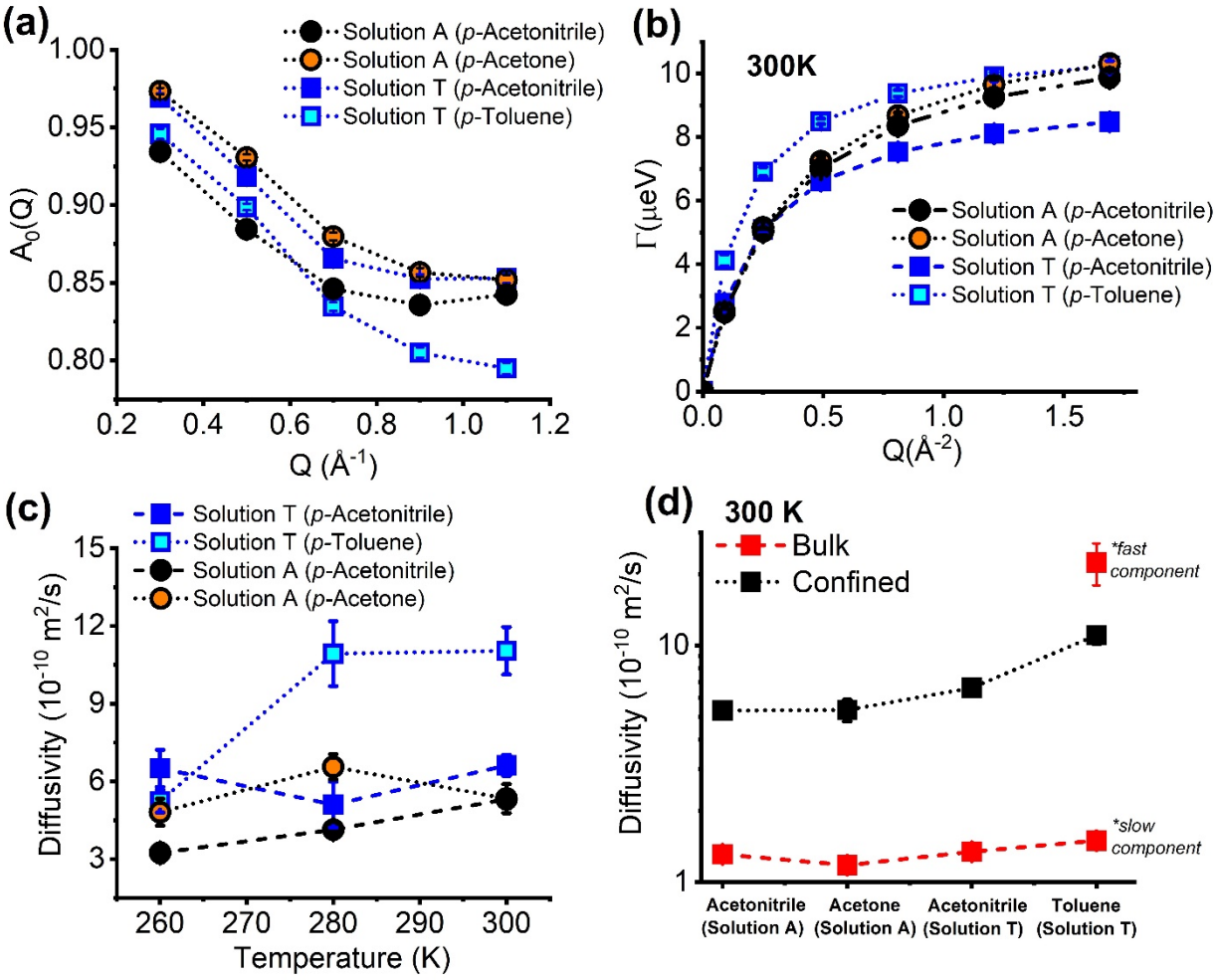

Fig. 4. In (a), the evolution of $A_0(Q)$ at 300K is presented for acetonitrile and the co-solvents in Solutions A and T. (b) shows the fits of Γ(Q) obtained at 300 K with eq. 3 and (c) shows the diffusion coefficients calculated for the solutions at different temperatures. (d) presents a comparison between the diffusion coefficients calculated for the solutions under confinement at 300 K and those calculated in ref. [27] for the bulk solutions. For toluene in Solution T, two components (fast and slow) had to be used in ref. [27] to properly describe the QENS data.

Since our main focus is to untangle the mechanisms behind the electrochemical performances of Solutions A and T, we mostly focus on the diffusivities at 300 K. In Solution A, *p*-acetonitrile and *p*-acetone have very similar diffusivities, which indicates that, on average, they are either involved in solvation complexes with similar dimensions, diffuse together as part of the same solvation complexes, or even diffuse as free particles through similar paths within the AMC hierarchical structure. The first two hypotheses are more plausible for various reasons. First, the

diffusion coefficients of the neat solvents are much higher than those observed herein (e.g. ~ 40 x 10^{-10} m^2/s for acetonitrile[40]). Also, the dynamics of *p*-acetonitrile and *p*-acetone are activated at the same temperature, as shown in Fig.3b. In contrast, in Solution T, the average diffusivity of *p*-toluene is nearly twice higher than *p*-acetonitrile's showing that, while acetonitrile is still strongly involved in ionic solvation, the mobile molecules of toluene are much less affected by either the presence of ions or the electrode walls.

The above-proposed scenario is reinforced by comparing the diffusivities obtained under confinement with those from the bulk solutions (extracted from ref. [27]), as displayed in Fig. 4d. In Solution A, the diffusivities obtained under confinement are much higher, as well as for *p*-acetonitrile in Solution T (the case of *p*-Toluene is discussed below). While this outcome is somewhat counterintuitive, it has been previously observed (mainly in ionic liquids)[41, 42] and, as mentioned above, associated with the large fraction of molecules immobilized by the confinement matrix. That is, the remaining mobile molecules are prevented from interacting with the carbon walls, which favors the increase in the measurable diffusivity. Also, as most of the solvent is attached to the pore surfaces, the remaining mobile phases are expected to have viscosities and solvation structures distinct from those in the bulk solutions. In particular, the higher diffusivities under confinement suggest a partial disruption of the solvation complexes once found in the bulk solutions, which may be critical for the ion/electrode direct interactions and the balance between surface and diffusion-controlled charge storage mechanisms.[43-45]

In the case of *p*-toluene, our previous analysis of the unconfined Solution T showed that $S(Q, \omega)$ could not be described by a single component, even considering a stretched function.[27] In that case, two Lorentzian functions were used and exposed the presence of a slower population of the co-solvent, whose dynamics is influenced by the presence of ions, and a fraction of *p*-toluene

performing freer and faster motions.[27] In Fig. 4d, the diffusivities of both populations are shown, and the diffusivity obtained under confinement approaches that of the freer *p*-toluene molecules. In other words, the participation of toluene in ion coordination becomes more sluggish under confinement and this effect can be decisive in improving the diffusion-controlled charge storage mechanisms. On the one hand, one can, for example, hypothesize that this improvement is driven by the increase in the overall entropy of the system led by toluene's mobility, which could favor the transit of ions to the electrode's surfaces. On the other hand, one could also reasonably argue that the presented scenario with the poorly interacting co-solvent leads to a highly concentrated acetonitrile/LiTFSI domains, whose low entropy should ultimately hinder ionic mobility.[46, 47] Therefore, a more precise picture of this matter must be sought in future works combining experimental and theoretical approaches.

In conclusion, we combined SPECS and QENS to understand how different co-solvents, with low and moderate dielectric constants - toluene and acetone - influence the charge storage mechanisms in a system formed by a concentrated LiTFSI/acetonitrile electrolyte in activated carbon electrodes. With SPECS, we showed that the presence of acetone favors the occurrence of surface-controlled mechanisms while toluene allows for greater contribution from diffusive-controlled processes. These results were rationalized with QENS, which revealed that toluene does interact with the electrode walls and competes with charged species to populate the AMC's hierarchical structure. In comparison with acetone, the presence of toluene in the carbon walls is less detrimental to the interactions between the cations and the functional groups of the electrodes and the subsequent Faradaic reactions. The discrepancies in the contributions from diffusion-controlled mechanisms provided by Solutions A and T can also be associated with changes in the solvation structures under confinement. On the one hand, in Solution A, acetonitrile and acetone

are very likely to concomitantly participate in the ionic solvation, as in the bulk solution. On the other hand, any interaction of toluene with the solvation structures is weaker under confinement than in the bulk solution. Hence, we envisage a more drastic change in the overall configuration of the solvation sheaths which may be crucial to promote the diffusion-controlled mechanisms. This analysis would greatly benefit from future works combining experimental and theoretical approaches to reveal the solvation structures under confinement and the correspondent impacts in ions adsorption on the AMC's surfaces.

ASSOCIATED CONTENT

Supporting Information

The Supporting Information is available free of charge on the ACS Publications website.
Additional details of the synthesis of the mesoporous carbon, preparation of electrolytes, electrode preparation, electrochemical protocol, and the SPECS and QENS experiments are presented. Supporting data of SPECS and QENS are also available.

AUTHOR INFORMATION

Corresponding Authors

* M. L. Martins. E-mail: martinsml@ornl.gov.
* E. Mamontov. E-mail: mamontove@ornl.gov.

Author Contributions

MLM and EM performed the QENS experiments and data analysis. TW and SD were responsible for the electrochemical characterization.

Notes

The authors declare no competing financial interests.

ACKNOWLEDGMENT

This research used resources at the Spallation Neutron Source (IPTS 27122) and Center for Nanophase Materials Sciences, DOE Office of Science User Facilities operated by the Oak Ridge National Laboratory (ORNL). This work was supported as part of the Fluid Interface Reactions, Structures and Transport (FIRST) Center, an Energy Frontier Research Center funded by the U.S. Department of Energy, Office of Science, Office of Basic Energy Sciences. This research used resources of the National Energy Research Scientific Computing Center (NERSC), a DOE Office of Science User Facility supported by the Office of Science of the U.S. Department of Energy under Contract No. DE-AC0205CH11231. ORNL is managed by UT-Battelle, LLC, for U.S. DOE under Contract No. DEAC05-00OR22725.

References

(1) Fleischmann, S.; Mitchell, J. B.; Wang, R.; Zhan, C.; Jiang, D.-e.; Presser, V.; Augustyn, V. Pseudocapacitance: From Fundamental Understanding to High Power Energy Storage Materials. *Chemical Reviews* **2020**, *120* (14), 6738-6782. DOI: 10.1021/acs.chemrev.0c00170.

(2) Schoetz, T.; Gordon, L. W.; Ivanov, S.; Bund, A.; Mandler, D.; Messinger, R. J. Disentangling faradaic, pseudocapacitive, and capacitive charge storage: A tutorial for the characterization of batteries, supercapacitors, and hybrid systems. *Electrochimica Acta* **2022**, *412*. DOI: 10.1016/j.electacta.2022.140072.

(3) Fleischmann, S.; Zhang, Y.; Wang, X. P.; Cummings, P. T.; Wu, J. Z.; Simon, P.; Gogotsi, Y.; Presser, V.; Augustyn, V. Continuous transition from double-layer to Faradaic charge storage in confined electrolytes. *Nat Energy* **2022**, *7* (3), 222-228. DOI: 10.1038/s41560-022-00993-z.

(4) Ge, K.; Shao, H.; Raymundo-Piñero, E.; Taberna, P.-L.; Simon, P. Cation desolvation-induced capacitance enhancement in reduced graphene oxide (rGO). *Nat Commun* **2024**, *15* (1). DOI: 10.1038/s41467-024-46280-1.

(5) Prehal, C.; Koczwara, C.; Jäckel, N.; Schreiber, A.; Burian, M.; Amenitsch, H.; Hartmann, M. A.; Presser, V.; Paris, O. Quantification of ion confinement and desolvation in nanoporous carbon supercapacitors with modelling and in situ X-ray scattering. *Nat Energy* **2017**, *2* (3). DOI: 10.1038/nenergy.2016.215.

(6) Yoshida, K.; Nakamura, M.; Kazue, Y.; Tachikawa, N.; Tsuzuki, S.; Seki, S.; Dokko, K.; Watanabe, M. Oxidative-Stability Enhancement and Charge Transport Mechanism in Glyme-Lithium Salt Equimolar Complexes. *Journal of the American Chemical Society* **2011**, *133* (33), 13121-13129. DOI: 10.1021/ja203983r.

(7) Suo, L. M.; Hu, Y. S.; Li, H.; Armand, M.; Chen, L. Q. A new class of Solvent-in-Salt electrolyte for high-energy rechargeable metallic lithium batteries. *Nat Commun* **2013**, *4*. DOI: 10.1038/ncomms2513.

(8) Suo, L. M.; Borodin, O.; Gao, T.; Olguin, M.; Ho, J.; Fan, X. L.; Luo, C.; Wang, C. S.; Xu, K. "Water-in-salt" electrolyte enables high-voltage aqueous lithium-ion chemistries. *Science* **2015**, *350* (6263), 938-943. DOI: 10.1126/science.aab1595.

(9) Yamada, Y.; Wang, J. H.; Ko, S.; Watanabe, E.; Yamada, A. Advances and issues in developing salt-concentrated battery electrolytes (vol 4, pg 269, 2019). *Nat Energy* **2019**, *4* (5), 427-427. DOI: 10.1038/s41560-019-0375-5.

(10) Xiang, L.; Ou, X.; Wang, X.; Zhou, Z.; Li, X.; Tang, Y. Highly Concentrated Electrolyte towards Enhanced Energy Density and Cycling Life of Dual-Ion Battery. *Angewandte Chemie International Edition* **2020**, *59* (41), 17924-17930. DOI: 10.1002/anie.202006595.

(11) Li, J.; Han, C.; Ou, X.; Tang, Y. Concentrated Electrolyte for High-Performance Ca-Ion Battery Based on Organic Anode and Graphite Cathode. *Angewandte Chemie* **2022**, *134* (14). DOI: 10.1002/ange.202116668.

(12) Borodin, O.; Self, J.; Persson, K. A.; Wang, C. S.; Xu, K. Uncharted Waters: Super-Concentrated Electrolytes. *Joule* **2020**, *4* (1), 69-100. DOI: 10.1016/j.joule.2019.12.007.

(13) Elliott, G. R.; Gregory, K. P.; Robertson, H.; Craig, V. S. J.; Webber, G. B.; Wanless, E. J.; Page, A. J. The known-unknowns of anomalous underscreening in concentrated electrolytes. *Chemical Physics Letters* **2024**, *843*. DOI: 10.1016/j.cplett.2024.141190.

(14) Wang, Y.; Hao, X.; Kang, Y.; Dong, M.; Fang, Z.; Hu, Y.; Wang, H.; Fan, X.; Yan, Y.; Ye, Z.; et al. Enhanced ion conductivity of “water-in-salt” electrolytes by nanochannel membranes. *Journal of Materials Chemistry A* **2023**, *11* (3), 1394-1402. DOI: 10.1039/d2ta08244f.

(15) Wang, X.; Mathis, T. S.; Sun, Y.; Tsai, W.-Y.; Shpigel, N.; Shao, H.; Zhang, D.; Hantanasirisakul, K.; Malchik, F.; Balke, N.; et al. Titanium Carbide MXene Shows an Electrochemical Anomaly in Water-in-Salt Electrolytes. *ACS Nano* **2021**, *15* (9), 15274-15284. DOI: 10.1021/acsnano.1c06027.
(16) Meisner, Q. J.; Rojas, T.; Glossmann, T.; Hintennach, A.; Liu, Q.; Cao, J.; Redfern, P. C.; Ngo, A. T.; Curtiss, L. A.; Zhang, Z. Impact of Co-Solvent and LiTFSI Concentration on Ionic Liquid-Based Electrolytes for Li-S Battery. *J Electrochem Soc* **2020**, *167* (7). DOI: 10.1149/1945-7111/ab76a3.
(17) Dokko, K.; Tachikawa, N.; Yamauchi, K.; Tsuchiya, M.; Yamazaki, A.; Takashima, E.; Park, J.-W.; Ueno, K.; Seki, S.; Serizawa, N.; et al. Solvate Ionic Liquid Electrolyte for Li–S Batteries. *J Electrochem Soc* **2013**, *160* (8), A1304-A1310. DOI: 10.1149/2.111308jes.
(18) Zheng, J. M.; Chen, S. R.; Zhao, W. G.; Song, J. H.; Engelhard, M. H.; Zhang, J. G. Extremely Stable Sodium Metal Batteries Enabled by Localized High-Concentration Electrolytes. *Acs Energy Lett* **2018**, *3* (2), 315-321. DOI: 10.1021/acsenergylett.7b01213.
(19) Doi, T.; Shimizu, Y.; Hashinokuchi, M.; Inaba, M. Dilution of Highly Concentrated LiBF4/Propylene Carbonate Electrolyte Solution with Fluoroalkyl Ethers for 5-V LiNi0.5Mn1.5O4Positive Electrodes. *J Electrochem Soc* **2017**, *164* (1), A6412-A6416. DOI: 10.1149/2.0611701jes.
(20) Yamada, Y.; Wang, J.; Ko, S.; Watanabe, E.; Yamada, A. Advances and issues in developing salt-concentrated battery electrolytes. *Nat Energy* **2019**, *4* (4), 269-280. DOI: 10.1038/s41560-019-0336-z.
(21) Liu, X.; Mariani, A.; Adenusi, H.; Passerini, S. Locally Concentrated Ionic Liquid Electrolytes for Lithium-Metal Batteries. *Angewandte Chemie* **2023**, *135* (17). DOI: 10.1002/ange.202219318.
(22) Liu, J.; Zhou, Y.; Yan, T.; Gao, X. P. Perspectives of High‐Performance Li–S Battery Electrolytes. *Adv Funct Mater* **2023**, *34* (4). DOI: 10.1002/adfm.202309625.
(23) Xu, C.; Diemant, T.; Liu, X.; Passerini, S. Locally Concentrated Deep Eutectic Liquids Electrolytes for Low-Polarization Aluminum Metal Batteries. *Advanced Materials* **2024**. DOI: 10.1002/adma.202400263.
(24) Wang, J.; Buzolic, J. J.; Mullen, J. W.; Fitzgerald, P. A.; Aman, Z. M.; Forsyth, M.; Li, H.; Silvester, D. S.; Warr, G. G.; Atkin, R. Nanostructure of Locally Concentrated Ionic Liquids in the Bulk and at Graphite and Gold Electrodes. *ACS Nano* **2023**, *17* (21), 21567-21584. DOI: 10.1021/acsnano.3c06609.
(25) Liu, X.; Passerini, S. Locally Concentrated Ionic Liquid Electrolytes for Lithium/Sulfurized Polyacrylonitrile Batteries. *ECS Meeting Abstracts* **2023**, *MA2023-02* (2), 365-365. DOI: 10.1149/MA2023-022365mtgabs.
(26) Ren, X. D.; Chen, S. R.; Lee, H.; Mei, D. H.; Engelhard, M. H.; Burton, S. D.; Zhao, W. G.; Zheng, J. M.; Li, Q. Y.; Ding, M. S.; et al. Localized High-Concentration Sulfone Electrolytes for High-Efficiency Lithium-Metal Batteries. *Chem-Us* **2018**, *4* (8), 1877-1892. DOI: 10.1016/j.chempr.2018.05.002.
(27) Martins, M. L.; Lin, X. B.; Gainaru, C.; Keum, J. K.; Cummings, P. T.; Sokolov, A. P.; Sacci, R. L.; Mamontov, E. Structure-Dynamics Interrelation Governing Charge Transport in Cosolvated Acetonitrile/LiTFSI Solutions. *J Phys Chem B* **2023**, *127* (1), 308-320. DOI: 10.1021/acs.jpcb.2c07327.
(28) Martins, M. L.; Sacci, R. L.; Lin, X. B.; Matsumoto, R.; Popov, I.; Cui, J. L.; Kobayashi, T.; Tyagi, M.; Guo, W.; Dai, S.; et al. Beyond Simple Dilution: Superior Conductivities from Cosolvation of Acetonitrile/LiTFSI Concentrated Solution with Acetone. *J Phys Chem C* **2022**, *126* (5), 2788-2796. DOI: 10.1021/acs.jpcc.1c09352.
(29) Martins, M. L.; Sacci, R. L.; Sanders, N. C.; Tyler, J. L.; Matsumoto, R.; Popov, I.; Guo, W.; Dai, S.; Cummings, P. T.; Sokolov, A. P.; et al. Addition of Chloroform in a Solvent-in-Salt Electrolyte: Outcomes in the Microscopic Dynamics in Bulk and Confinement. *J Phys Chem C* **2020**, *124* (41), 22366-22375. DOI: 10.1021/acs.jpcc.0c05311.
(30) Ren, X.; Chen, S.; Lee, H.; Mei, D.; Engelhard, M. H.; Burton, S. D.; Zhao, W.; Zheng, J.; Li, Q.; Ding, M. S.; et al. Localized High-Concentration Sulfone Electrolytes for High-Efficiency Lithium-Metal Batteries. *Chem-Us* **2018**, *4* (8), 1877-1892. DOI: 10.1016/j.chempr.2018.05.002.
(31) Wang, T.; Sacci, R. L.; Liang, J. Y.; Do-Thanh, C. L.; Fan, J. T.; Chen, H.; Sun, Y. F.; Thapaliya, B. P.; Mahurin, S. M.; Zhou, M. S.; et al. Mechanistic Insights of Pore Contributions in Carbon Supercapacitors

by Modified Step Potential Electrochemical Spectroscopy. *J Electrochem Soc* **2021**, *168* (6). DOI: 10.1149/1945-7111/ac099a.
(32) Wang, T.; Pan, R. T.; Martins, M. L.; Cui, J. L.; Huang, Z. N.; Thapaliya, B. P.; Do-Thanh, C. L.; Zhou, M. S.; Fan, J. T.; Yang, Z. Z.; et al. Machine-learning-assisted material discovery of oxygen-rich highly porous carbon active materials for aqueous supercapacitors. *Nat Commun* **2023**, *14* (1). DOI: 10.1038/s41467-023-40282-1.
(33) Osti, N. C.; Mamontov, E. Microscopic dynamics in room-temperature ionic liquids confined in materials for supercapacitor applications. *Sustainable Energy & Fuels* **2020**, *4* (4), 1554-1576. DOI: 10.1039/c9se00829b.
(34) Bée, M. Quasielastic neutron scattering:: Introduction and general principles. *J Phys Iv* **2000**, *10* (P1), 1-14. DOI: DOI 10.1051/jp4:2000101.
(35) Mamontov, E.; Herwig, K. W. A time-of-flight backscattering spectrometer at the Spallation Neutron Source, BASIS. *Rev Sci Instrum* **2011**, *82* (8). DOI: 10.1063/1.3626214.
(36) Scott, D. W.; Berg, W. T.; Messerly, J. F.; Mccullough, J. P.; Todd, S. S.; Hossenlopp, I. A.; Guthrie, G. B. Toluene - Thermodynamic Properties, Molecular Vibrations, and Internal Rotation. *J Phys Chem-Us* **1962**, *66* (5), 911-&. DOI: DOI 10.1021/j100811a038.
(37) Vatamanu, J.; Borodin, O.; Smith, G. D. Molecular Dynamics Simulation Studies of the Structure of a Mixed Carbonate/LiPF Electrolyte near Graphite Surface as a Function of Electrode Potential. *J Phys Chem C* **2012**, *116* (1), 1114-1121. DOI: 10.1021/jp2101539.
(38) Arbe, A.; Ramirez-Cuesta, A.; Smith, R.; Mamontov, E.; Cheng, Y.; Colmenero, J. ICE-MAN the Integrated Computational Environment for Modeling and Analysis for Neutrons at ORNL. *EPJ Web of Conferences* **2022**, *272*. DOI: 10.1051/epjconf/202227201013.
(39) Teixeira, J.; Bellissentfunel, M. C.; Chen, S. H.; Dianoux, A. J. Experimental-Determination of the Nature of Diffusive Motions of Water-Molecules at Low-Temperatures. *Phys Rev A* **1985**, *31* (3), 1913-1917. DOI: DOI 10.1103/PhysRevA.31.1913.
(40) Kovacs, H.; Kowalewski, J.; Laaksonen, A. Molecular-Dynamics Simulation of Liquid-Mixtures of Acetonitrile and Chloroform. *J Phys Chem-Us* **1990**, *94* (19), 7378-7385. DOI: DOI 10.1021/j100382a013.
(41) Bridges, C. A.; Martins, M. L.; Jafta, C. J.; Sun, X. G.; Paranthaman, M. P.; Liu, J.; Dai, S.; Mamontov, E. Dynamics of Emim+ in [Emim][TFSI]/LiTFSI Solutions as Bulk and under Confinement in a Quasi-liquid Solid Electrolyte. *The Journal of Physical Chemistry B* **2021**, *125* (20), 5443-5450. DOI: 10.1021/acs.jpcb.1c02383.
(42) Berrod, Q.; Ferdeghini, F.; Judeinstein, P.; Genevaz, N.; Ramos, R.; Fournier, A.; Dijon, J.; Ollivier, J.; Rols, S.; Yu, D.; et al. Enhanced ionic liquid mobility induced by confinement in 1D CNT membranes. *Nanoscale* **2016**, *8* (15), 7845-7848. DOI: 10.1039/c6nr01445c.
(43) Ando, Y.; Okubo, M.; Yamada, A.; Otani, M. Capacitive versus Pseudocapacitive Storage in MXene. *Adv Funct Mater* **2020**, *30* (47). DOI: 10.1002/adfm.202000820.
(44) Kim, K.; Okubo, M.; Yamada, A. Interfacial Dissociation of Contact-Ion-Pair on MXene Electrodes in Concentrated Aqueous Electrolytes. *J Electrochem Soc* **2019**, *166* (15), A3739-A3744. DOI: 10.1149/2.0931915jes.
(45) Lu, Z. Y.; Geng, C. N.; Yang, H. J.; He, P.; Wu, S. C.; Yang, Q. H.; Zhou, H. S. Step-by-step desolvation enables high-rate and ultra-stable sodium storage in hard carbon anodes. *P Natl Acad Sci USA* **2022**, *119* (40). DOI: 10.1073/pnas.2210203119.
(46) Kobayashi, T.; Kemna, A.; Fyta, M.; Braunschweig, B.; Smiatek, J. Aqueous Mixtures of Room-Temperature Ionic Liquids: Entropy-Driven Accumulation of Water Molecules at Interfaces. *J Phys Chem C* **2019**, *123* (22), 13795-13803. DOI: 10.1021/acs.jpcc.9b04098.
(47) Jeon, J.; Kim, H.; Goddard, W. A.; Pascal, T. A.; Lee, G. I.; Kang, J. K. The Role of Confined Water in Ionic Liquid Electrolytes for Dye-Sensitized Solar Cells. *J Phys Chem Lett* **2012**, *3* (4), 556-559. DOI: 10.1021/jz3000036.